

Article

Evaluation of Unified Algorithms for Remote Sensing of Chlorophyll-a and Turbidity in Lake Shinji and Lake Nakaumi of Japan and the Vaal Dam Reservoir of South Africa under Eutrophic and Ultra-Turbid Conditions

Yuji Sakuno ^{1,*} , Hiroshi Yajima ² , Yumi Yoshioka ³, Shogo Sugahara ⁴,
Mohamed A. M. Abd Elbasit ^{5,6}, Elhadi Adam ⁶ and Johannes George Chirima ⁵

¹ Graduate School of Engineering, Hiroshima University, Higashihiroshima 739-8527, Japan

² Estuary Research Center, Shimane University, Matsue 690-8504, Japan; yajima@soc.shimane-u.ac.jp

³ Faculty of Agriculture, Tottori University, Tottori 680-8550, Japan; yoshioka@tottori-u.ac.jp

⁴ Graduate School of Science and Engineering, Shimane University, Matsue 690-8504, Japan; suga@riko.shimane-u.ac.jp

⁵ Agricultural Research Council-Institute for Soil, Climate and Water, Pretoria 0001, South Africa; mohamedahmedm@arc.agric.za (M.A.M.A.E.); ChirimaJ@arc.agric.za (J.G.C.)

⁶ School of Geography, Archaeology and Environmental Studies, University of the Witwatersrand, Johannesburg 2000, South Africa; elhadi.adam@wits.ac.za

* Correspondence: sakuno@hiroshima-u.ac.jp; Tel.: +81-82-424-7773

Received: 19 April 2018; Accepted: 8 May 2018; Published: 9 May 2018



Abstract: We evaluated unified algorithms for remote sensing of chlorophyll-a (Chla) and turbidity in eutrophic and ultra-turbid waters such as Japan's Lake Shinji and Lake Nakaumi (SJNU) and the Vaal Dam Reservoir (VDR) in South Africa. To realize this objective, we used 38 remote sensing reflectance (R_{rs}), Chla and turbidity datasets collected in these waters between July 2016 and March 2017. As a result, we clarified the following items. As a unified Chla model, we obtained strong correlation ($R^2 = 0.7$, RMSE = 2 mg m⁻³) using a two-band model (2-BM) and three-band model (3-BM), with $R_{rs}(687)/R_{rs}(672)$ and $[R_{rs}^{-1}(687) - R_{rs}^{-1}(672)] \times R_{rs}(832)$. As a unified turbidity model, we obtained strong correlation ($R^2 = 0.7$, RMSE = 260 NTU) using 2-BM and 3-BM, with $R_{rs}(763)/R_{rs}(821)$ and $R_{rs}(810) - [R_{rs}(730) + R_{rs}(770)]/2$. When targeting the Sentinel-2 Multispectral Imager (MSI) frequency band, we focused on MSI Bands 4 and 5 ($R_{rs}(740)$ and $R_{rs}(775)$) for the Chla algorithm. When optically separating SJNU and VDR data, it is effective to use the slopes of MSI Bands 3 and 4 ($R_{rs}(560)$ and $R_{rs}(665)$) and the slopes of MSI Bands 7 and 9 ($R_{rs}(775)$ and $R_{rs}(865)$).

Keywords: chlorophyll; turbidity; remote sensing; reflectance; lake; reservoir; Sentinel-2

1. Introduction

Fresh water on land, such as in rivers, lakes and reservoirs, accounts for about 0.01% of Earth's water [1]; thus, protecting this resource is a vital global issue. In particular, monitoring water quality to detect turbid water and algal blooms is indispensable [2]. In this research, we focus on the waters of Japan's Lake Shinji and Lake Nakaumi (SJNU), which are well known as brackish water zones with abundant fishery and sightseeing resources such as birds and clams. To protect these resources, water quality monitoring has been conducted at fixed points for a long time [3–7]. However, recent years have seen abnormal phenomena in water bodies such as cyanobacteria bloom, red tide, dysoxic bottom water and the sudden occurrence of seagrass [8,9]. We also focus on a second research site in this study,

the Vaal Dam Reservoir (VDR) in South Africa, which is among the largest reservoirs in South Africa. The Vaal Dam was constructed in 1938 and plays a crucial role in supplying irrigation and industrial water to the Johannesburg metropolitan area [10,11]. For this reason, water quality has been conducted for a long time [12,13]. However, recent years have seen a further increase in the importance of water quality monitoring because of problems such as acidic mine drainage [14,15], increased water demand due to urbanization and uneven rainfall distribution caused by climate change [16]. Thus, SJNU and VDR have both similar historical backgrounds and current problems, so it is worth collaborating to improve the water quality monitoring techniques of both sites. Moreover, the current situation cannot be dealt with using conventional point source monitoring; thus, it is vital to establish technology such as remote sensing that can simultaneously monitor wide areas. Conventional water quality remote sensing relies mainly on algorithms dealing with blue and green light, but in optically-complex inland waters, the red and near-infrared parts of the spectrum are often used [17]. For example, methods such as two-band algorithms [18,19], three-band algorithms [20,21] and four-band algorithms [22,23] have been proposed to measure chlorophyll-a (Chla). For measuring turbidity (Turb) or total suspended solids (TSS), which is an indicator of turbidity, methods such as one-band algorithms [24,25] and two-band algorithms [26,27] have been proposed. Furthermore, Chla and turbidity algorithms, such as SCI (Synthetic Chlorophyll Index), which applied fluorescence line height [28] using the fluorescence band for more turbid conditions and a turbidity algorithm [29] using an 810-nm reflection peak under rich colored dissolved organic matter (CDOM) conditions, have been proposed. Several algorithms have been proposed for inland water, but a unified approach has not yet been established.

Based on the current state of satellite sensors, monitoring inland water quality using sensors such as the Moderate Resolution Imaging Spectroradiometer (MODIS) aboard the Terra and Aqua satellites, the Geostationary Ocean Color Imager (GOCI) aboard the Communication, Ocean and Meteorological Satellite and the Medium Resolution Imaging Spectrometer (MERIS) aboard the Envisat satellite, which have spatial resolutions of 500 m or better, high frequencies and high spectral resolutions, has become popular since 2000 [30–32]. Among these, MERIS, which operated from 2002–2012, used a 600–900 nm band to effectively monitor the quality of optically-complex inland water. Moreover, with an improved spatial resolution, continuous observation of small water bodies is possible with the same spectral performance. The Multispectral Imager (MSI) of the recent Sentinel-2A mission, which was launched in June 2015, has a 10–60-m spatial resolution, a 10-day repeat cycle and uses a 600–900-nm band that can be used for effective water quality monitoring. Additionally, high-resolution hyperspectral imagers, such as EO-1's Hyperion (2000–2017), the Hyperspectral Imager for the Coastal Ocean (HICO) (2009–2014), which was installed on the International Space Station (ISS), and the Hyperspectral Imager Suite, which is scheduled to be operated on the ISS in 2019, also exist. Water quality monitoring for large rivers such as the Mississippi River using airborne hyperspectral sensors has been also conducted [33]. In addition to algorithms that do not depend on band position for inland waters with complex optical properties, these hyperspectral data will become important in the future.

Therefore, in this study, we evaluated recent water quality algorithms using field observation data for spectral reflectance, Chla and Turb) in SJNU and VDR under eutrophic and ultra-turbid conditions to assess algorithm stability.

2. Materials and Methods

2.1. Study Area and Field Survey

Table 1 shows the research area's basic specifications. SJNU consists of brackish lakes located on the border between Japan's Shimane and Tottori prefectures. The two lakes are connected by the 7.3 km-long Ohashi River and the main freshwater stream flows from the Hii River (accounting for about 90% Lake Shinji's freshwater origin). Freshwater flows from the Hii River, through Lake Shinji and the Ohashi River into Lake Nakaumi and into the Sea of Japan via Miho Bay. The salinity of Lake Shinji and Lake Nakaumi is about 0.3% and about 10%, respectively, with Lake Nakaumi, which is

close to the Sea of Japan, having a strong salinity layer developed in some places. Both lakes have an average transparency of about 1 m, with high phytoplankton and suspended solid concentrations. In addition, cyanobacteria (blue-green algae) and red tide blooms often occur in Lake Shinji and Lake Nakaumi, respectively. The SJNU catchment area's average annual rainfall is about 1700–2300 mm.

VDR is a freshwater dam reservoir 56 km south of Johannesburg, South Africa. This dam is at the Vaal River drainage system, which has a catchment area entirely situated within South Africa. The name Vaal means gray-brown in Afrikaans, and the VDR is characterized by highly turbid water (known as ultra-turbid conditions). The VDR catchment area's average annual rainfall is about 700 mm.

Field surveys of SJNU were carried out on 15 July and 12 September 2016, and field surveys of VDR were conducted on 12 September and 26 October 2016. To measure Chla and Turb, we used Hydrolab Data Sonde 5× instruments (Chla sensor: range = 0.03–500 mg m⁻³, accuracy = ±3%, resolution = 0.01 mg m⁻³; turbidity sensor: range = 0–3000 NTU, accuracy = 1% (<100 NTU), 3% (100–400 NTU), 5% (>400 NTU), resolution = 0.1 NTU), and an MS 720 portable spectral radiometer produced by EKO Ltd. (Guangzhou, China) (spectral range = 350–1050 nm, sampling interval = 3.3 nm) was used to measure remote sensing reflectance (R_{rs}). We measured spectral irradiance both immediately above the water surface and of solar radiation reflected by a ZB 6010 white board (Japan Color Research Laboratory) three times. We determined the remote sensing reflectance (sr⁻¹) by calculating respective average reflectance and divided it by pi. The basic reflectance measurement method and R_{rs} transformation followed the method of Oyama et al. [34]. Mobley [35] and Tan et al. [36] point out the importance of removing sun and sky glint contained in R_{rs} . However, due to equipment and observation time, auxiliary observations such as sky radiance could not be conducted this time, so we did not make corrections for glint.

Table 1. Geographical characteristics of the target area.

	Area	Coast Line	Water Volume	Average Depth
Locations	(km ²)	(km)	(km ³)	(m)
Lake Shinji	79	48	0.34	4.5
Lake Nakaumi	86	64	0.36	5.4
Vaal Dam Reservoir	321	880	2.54	22.5

2.2. Chlorophyll-a and Turbidity Algorithms

Various remote sensing algorithms have been suggested to measure Chla and turbidity (or TSS) for inland waters with complex optical properties [17]. For example, the effectiveness of the following 2-band model (2-BM; hereinafter referred to as a C1 model) as a Chla algorithm has been shown using the red and near-infrared bands [18,19].

$$\text{Chla} \propto R_{rs}(\lambda_2) / R_{rs}(\lambda_1) \quad (1)$$

Recently, semi-analytical analytical models supported by the bio-optical theory have been proposed in waters that cannot be evaluated using Equation (1). For example, a 3-band model (3-BM; hereinafter referred to as a C2 model) and 4-band model (hereinafter referred to as a C3 model) [20–23] have been proposed. Here, we briefly explain these models according to bio-optical theory. R_{rs} observed immediately above the water surface can be expressed as:

$$R_{rs}(\lambda) \propto b_b(\lambda) / [a(\lambda) + b_b(\lambda)] \quad (2)$$

$$a(\lambda) = a_w(\lambda) + a_{cdom}(\lambda) + a_{chla}(\lambda) + a_{tripton}(\lambda) \quad (3)$$

$$b(\lambda) = b_w(\lambda) + b_p(\lambda) \quad (4)$$

where b_b is the water's backscattering coefficient; a_w , a_{chla} , a_{cdom} and $a_{tripton}$ are the absorption coefficients of pure water, phytoplankton, CDOM and inorganic suspended matter. It is relatively

easy to remotely estimate Chla in the open ocean because of the strong blue band absorption of Chla. However, Chla and CDOM from terrestrial origin both have strong blue band absorptions, making it difficult to remotely estimate Chla in inland water. Therefore, remote estimation in inland water relies on near-infrared bands, which have relatively small absorption for CDOM and similar a_{cdom} and $a_{tripton}$ values. Only a_{chla} , which is closely related to Chla, can be extracted by removing the influence of CDOM through relatively simple arithmetic operations. Figure 1 shows absorption coefficient spectral characteristics of underwater substances and four basic wavelengths (λ_1 , λ_2 , λ_3 and λ_4) typically used for Chla estimation.

The C2 model calculates a_{chla} depth by taking the difference between Chla absorption's maximum (λ_1) and minimum (λ_2) wavelengths, which is the reciprocal number of R_{rs} , and by multiplying Chla by R_{rs} near 740 nm, which is very small. This cancels the influence of b_b in the denominator.

$$\text{Chla} \propto [R^{-1}(\lambda_1) - R^{-1}(\lambda_2)][R(\lambda_3)] = [a_{chla}(\lambda_1) + a_w(\lambda_1) - a_w(\lambda_2)]/a_w(\lambda_3) \tag{5}$$

However, if the absorption component of the detritus (a_d) value that was omitted in Equation (3) is included, and thus cannot be ignored, Equation (5) may have a large error. Therefore, to alleviate the influence of a_d by using wavelengths in which a_d is assumed to have about the same range (for example, 720 nm and 750 nm), we replace $R^{-1}(\lambda_3)$ in Equation (5) with " $R^{-1}(\lambda_4) - R^{-1}(\lambda_3)$ " to create the following 4-band model.

$$\text{Chla} \propto [R^{-1}(\lambda_1) - R^{-1}(\lambda_2)][R^{-1}(\lambda_4) - R^{-1}(\lambda_3)]^{-1} = [a_{chla}(\lambda_1) + a_w(\lambda_1) - a_w(\lambda_2)]/[a_w(\lambda_4) - a_w(\lambda_3)] \tag{6}$$

Because λ_3 and λ_4 are close bands with similar optical characteristics, they are sometimes expressed as the following 3-BM.

$$\text{Chla} \propto [R^{-1}(\lambda_1) - R^{-1}(\lambda_2)][R^{-1}(\lambda_4) - R^{-1}(\lambda_3)]^{-1} = [a_{chla}(\lambda_1) + a_w(\lambda_1) - a_w(\lambda_2)]/[a_w(\lambda_3) - a_w(\lambda_2)] \tag{7}$$

In contrast, the turbidity algorithm uses an empirical single-band model (hereinafter referred to as the T1 model) [24,25] and a 2-BM (hereinafter referred to as the T2 model) [26,27] using red to near-infrared bands as follows.

$$\text{Turb} \propto R_{rs}(\lambda_5) \tag{8}$$

$$\text{Turb} \propto R_{rs}(\lambda_6)/R_{rs}(\lambda_7) \tag{9}$$

where Turb describes turbidity. Furthermore, in waters with a large CDOM influence, a 3-BM (hereinafter referred to as the T3 model) [29] with a high R_{rs} of 810 nm as an index has recently been proposed.

$$\text{Turb} \propto R_{rs}(\lambda_{10}) - [R_{rs}(\lambda_9) + R_{rs}(\lambda_{11})]/2 \tag{10}$$

In this paper, we validated the basic algorithm local data and the three Chla models and three turbidity models explained so far. Table 2 summarizes these algorithms.

Table 2. Summary of standard chlorophyll a (Chla) and turbidity algorithms used in this study. C, chlorophyll; T, turbidity.

Water Quality Parameters	Model Name	Algorithm Style	Original References
Chla	C1	$R_{rs}(\lambda_2)/R_{rs}(\lambda_1)$	[18,19]
	C2	$(R_{rs}(\lambda_1)^{-1} - R_{rs}(\lambda_2)^{-1}) \times R(\lambda_3)$	[20,21]
	C3	$[R_{rs}(\lambda_1)^{-1} - R_{rs}(\lambda_2)^{-1}]/[R_{rs}(\lambda_4)^{-1} - R_{rs}(\lambda_3)^{-1}]$	[22,23]
Turbidity	T1	$R(\lambda_5)$	[24,25]
	T2	$R(\lambda_6)/R(\lambda_7)$	[26,27]
	T3	$R(\lambda_8) - [R(\lambda_9) + R(\lambda_{10})]/2$	[29]

Representative bands: $\lambda_1 = 670$, $\lambda_2 = 710$, $\lambda_3 = 740$, $\lambda_4 = 750$, $\lambda_5 = 645$, $\lambda_6 = 850$, $\lambda_7 = 550$, $\lambda_8 = 810$, $\lambda_9 = 770$, $\lambda_{10} = 840$.

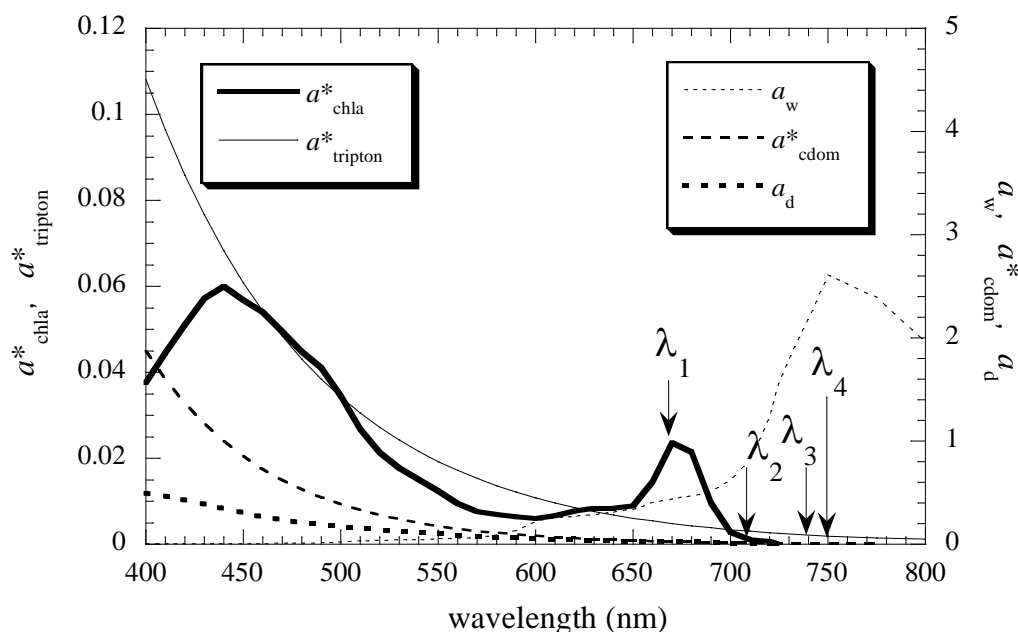


Figure 1. Typical absorption from Yang et al. [21] for a^*_{chl} , $a^*_{tripton}$, a_w , a^*_{cdom} . The a_d is from Kobayashi and Higa (private note) measured in Tokyo Bay.

2.3. Accuracy Assessment

To evaluate discrepancies between the model and measured values in Table 3, we calculated the root mean square error (RMSE), which is often used to assess accuracy during water quality remote sensing algorithm evaluation [21].

$$RMSE = \sqrt{\frac{\sum_{i=1}^N (WQ_{pred,i} - WQ_{meas,i})^2}{N}} \tag{11}$$

Here, N is the number of samples; $WQ_{pred,i}$ is the predicted value of Chla or turbidity; and $WQ_{meas,i}$ is the measured value of Chla or turbidity for each sample.

2.4. Simulated Satellite Data

To monitor Chla and turbidity using satellite data in the future, we simulated R_{rs} observed from each satellite data band using actual measurement data. Specifically, R_{rs} of the center wavelength for Sentinel-2 bands was extracted from the measurement R_{rs} data. However, because the normal Ocean Color sensor’s spatial resolution of 1 km is insufficient for monitoring on the scale of lakes and reservoirs, we used the Sentinel-2 MSI, which has a 10-m–30-m resolution. Table 3 shows MSI’s performance.

Table 3. Performance of the Sentinel-2 Multispectral Imager (MSI).

Satellite	Sensor	Launch	Spatial	
			Resolution (m)	Center Wavelength (nm)
Sentinel-2	MSI	February 2016	10/20*/60**	443**, 490, 560, 665, 705*, 740*, 775*, 842, 865*

3. Results

3.1. In Situ Measurements of Water Quality and R_{rs}

Figure 2 shows detailed sampling points (basic stationary point), and Appendix A lists all R_{rs} , Chla and turbidity data. Figure 3 shows the acquired spectral reflectance data. Measured Chla and turbidity data at a water depth of 0 m were used. Although SJNU and VDR had nearly identical Chla, VDR has turbidity values about 100- and 1000-times greater than SJNU, as shown in Table 4.

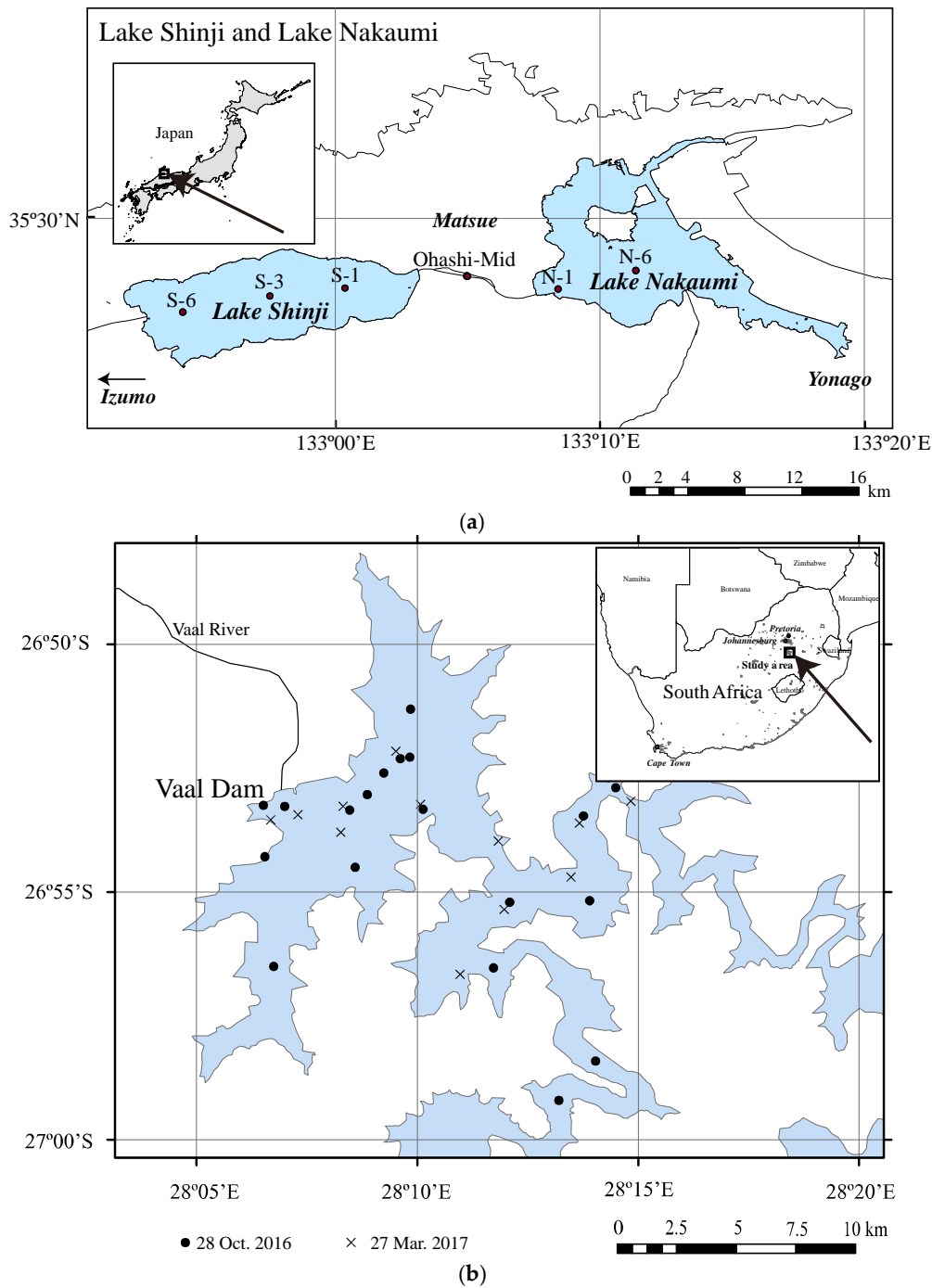


Figure 2. Study areas and field observation points. (a) Lake Shinji and Lake Nakaumi (SJNU); (b) Vaal Dam Reservoir (VDR).

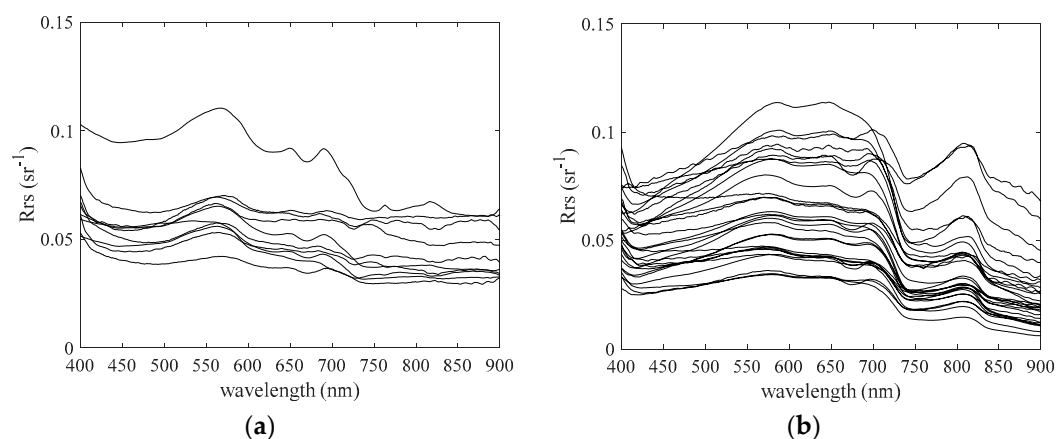


Figure 3. Acquired spectral reflectance (R_{rs}) characteristics. (a) Lake Shinji and Lake Nakaumi (SJNU); (b) Vaal Dam Reservoir (VDR).

Table 4. Chlorophyll-a (Chla) and turbidity range of field data.

Locations	Date	Chla		Turbidity		
		(mg m ⁻³)		(NTU)		N
		Min	Max	Min	Max	
L. Shinji and L. Nakaumi (SJNU)	15 July 2016 12 September 2016	4.7 0.8	19.8 12.5	2.1 0.0	5.9 2.3	6 4
Vaal Dam Reservoir (VDR)	26 October 2016 27 March 2017	2.1 3.0	13.8 4.6	386 106	1678 146	18 10

3.2. Algorithm Evaluation Using Field Spectra

3.2.1. Chla Algorithm

Determining the Chla algorithm's optimum wavelength position is vital for regional dependency reasons. Previous studies have confirmed changes in R^2 and RMSE values by moving the wavelength within a certain range [20,23]. Here, we selected the optimal band with the minimum RMSE as these studies; however, we tried all combinations of 1 nm in the 2-BM.

Figure 4 shows the Chla results from the C1 model in the SJNU and VDR. Figure 4a shows the correlation coefficient matrix $[R_{rs}(\lambda_1)/R_{rs}(\lambda_2)]$ and measured Chla derived every 1 nm in the 400–900-nm range. R_{rs} values at 687 nm and 672 nm are the highest correlated ($R^2 = 0.69$, RMSE mg m⁻³), and relatively strong correlation was obtained only in the narrow area noted by the box labeled "A." Figure 4b shows the optimal $[R_{rs}(687)/R_{rs}(672)]$ correlation and measured Chla. Figure 4c,d shows the RMSEs of variation between $[R_{rs}(\lambda_1)/R_{rs}(672)]$ or $[R_{rs}(687)/R_{rs}(\lambda_2)]$ and measured Chla when λ_1 or λ_2 is in the 600–900-nm range. Thus, in this model, we obtained a relatively stable RMSE of 1.95 ± 0.05 mg m⁻³ when λ_3 was about 740–900 nm, and the RMSE increases abruptly at wavelengths shorter than 740 nm.

Figure 5 shows the Chla results from the C2 model for in SJNU and VDR. Figure 5a shows RMSE variation between $[R_{rs}^{-1}(687) - R_{rs}^{-1}(672)] \times R(\lambda_3)$ and measured Chla when λ_3 is in the 600–900-nm range. Thus, in this model, we obtained a relatively stable RMSE of 1.95 ± 0.05 mg m⁻³ when λ_3 was about 740–900 nm, and the RMSE increases abruptly at wavelengths shorter than 740 nm. Figure 5b shows the optimal correlation between $[R_{rs}^{-1}(687) - R_{rs}^{-1}(672)] \times R(832)$ and measured Chla. As a result, we obtained a relatively high correlation ($R^2 = 0.73$, RMSE = 1.96 mg m⁻³) similar to that in Figure 4b. Moreover, compared the C2 model shows less variation that the C1 model when Chla concentrations are low (<5 mg m⁻³).

Figure 6 shows the Chla results of the C3 model in SJNU and VDR. Figure 6a shows RMSE variation between $[R_{rs}^{-1}(687) - R_{rs}^{-1}(672)] \times [R(\lambda_4) - R(832)]$ and measured Chla when λ_4 is in the 600–900-nm range. Figure 6b shows the optimal correlation between $[R_{rs}^{-1}(687) - R_{rs}^{-1}(672)] \times [R^{-1}(600) - R^{-1}(832)]$ and measured Chla. From these results, we determined that the RMSE within this wavelength range was 3.1–3.7 mg m^{-3} , and that estimation accuracy decreased in every band compared to the C2 model shown in Figure 4.

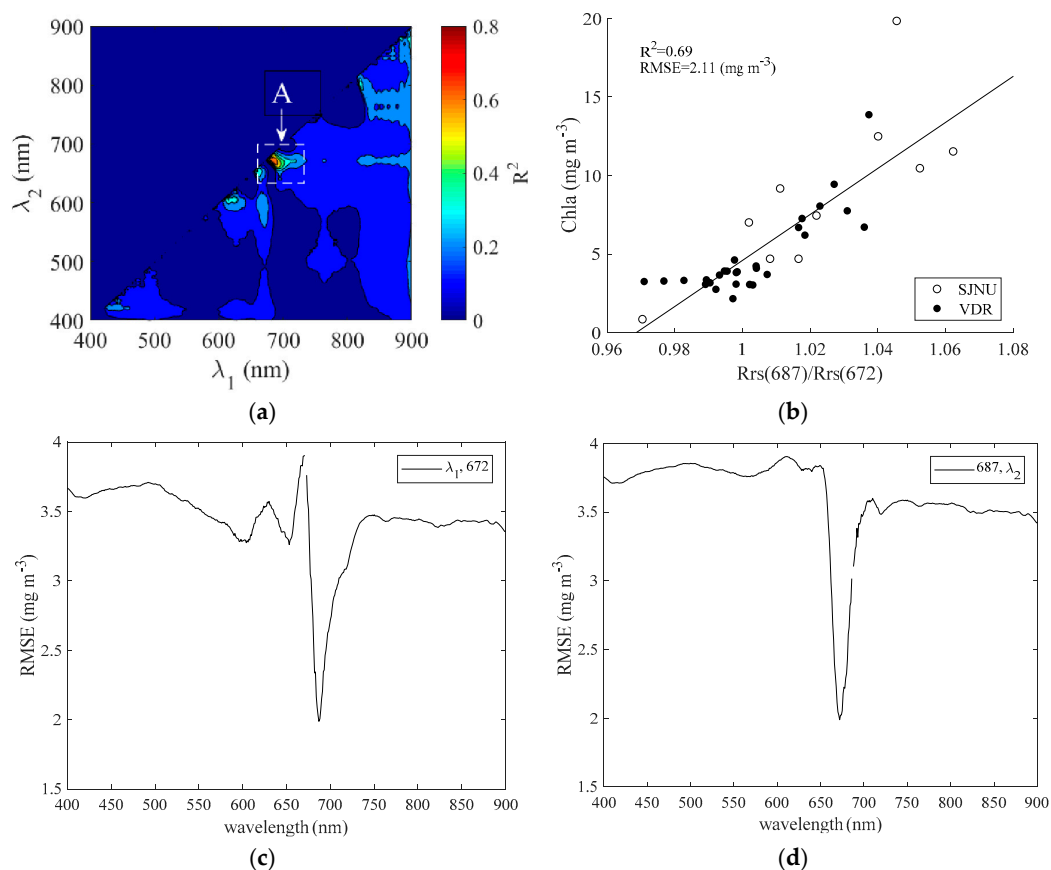


Figure 4. Chlorophyll a (Chla) results for the two-band model (C1) in Lake Shinji and Lake Nakaumi (SJNU) and the Vaal Dam Reservoir (VDR). (a) Correlation coefficient matrix between $[R_{rs}(\lambda_1)/R_{rs}(\lambda_2)]$ and measured Chla; (b) optimal correlation between $[R_{rs}(687)/R_{rs}(672)]$ and measured Chla; (c) root mean square error (RMSE) variation between $[R_{rs}(\lambda_1)/R_{rs}(672)]$ and measured Chla when λ_1 is in the 600–900-nm range; (d) RMSE variation between $[R_{rs}(687)/R_{rs}(\lambda_2)]$ and measured Chla when λ_2 is in the 600–900-nm range.

Table 5 shows the optimal Chla model produced using C1, C2 and C3 as summarized above. The Chla estimation error is smaller than the RMSE in the order of C2, C1 and C3.

Table 5. The optimal chlorophyll a (Chla) algorithm using the C1, C2 and C3 models.

Model		RMSE		
name	Algorithm	R ²	(mg m ⁻³)	n
C1	$\text{Chla} = 146.5 \times [R_{rs}(687)/R_{rs}(672)] - 141.9$	0.69	2.1	38
C2	$\text{Chla} = 245.2 \times [R_{rs}(687)^{-1} - R_{rs}(672)^{-1}] \times R_{rs}(832) + 4.266$	0.73	2.0	38
C3	$\text{Chla} = -0.1784 \times [R_{rs}(687)^{-1} - R_{rs}(672)^{-1}]/[R_{rs}(832)^{-1} - R_{rs}(600)^{-1}] + 5.777$	0.30	5.2	38

3.2.2. Turbidity Algorithm

As with the Chla algorithm, it is crucial to choose the turbidity algorithm’s optimal wavelength. Here, we performed optimal wavelength selection and evaluation using the same methods as were used with the Chla algorithm.

Figure 7 shows the turbidity results of the one-band model (T1) in SJNU and VDR. Figure 7a shows RMSE variation between $R_{rs}^{-1}(\lambda_5)$ and measured turbidity when λ_5 is in the 400–900-nm range. Figure 7b shows the optimal correlation ($R^2 = 0.17$, RMSE = 443 NTU) between $R_{rs}(814)$ and measured turbidity. This model’s estimation accuracy of 500 NTU or less was extremely bad.

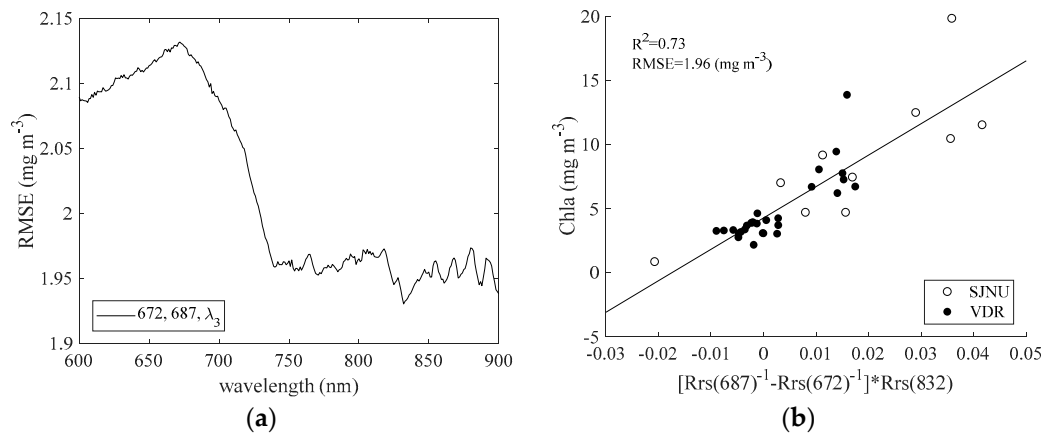


Figure 5. Chlorophyll a (Chla) results of the three-band model (C2) in Lake Shinji and Lake Nakaumi (SJNU) and the Vaal Dam Reservoir (VDR). (a) Root mean square error (RMSE) variation between $[R_{rs}^{-1}(687) - R_{rs}^{-1}(672)] \times R(\lambda_3)$ and measured Chla when λ_3 is in the 600–900-nm range; (b) optimal correlation between $[R_{rs}^{-1}(687) - R_{rs}^{-1}(672)] \times R(832)$ and measured Chla.

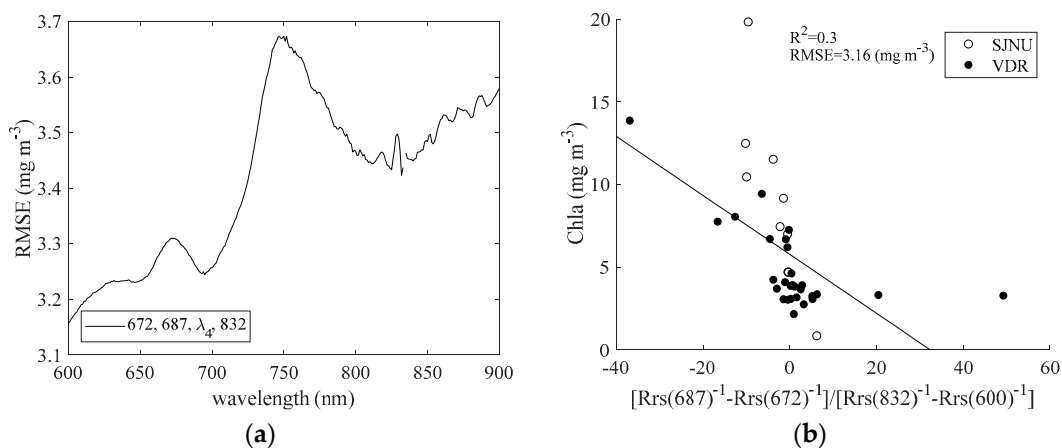


Figure 6. Chlorophyll a (Chla) results of the four-band model (C3) in Lake Shinji and Lake Nakaumi (SJNU) and the Vaal Dam Reservoir (VDR). (a) Root mean square error (RMSE) variation between $[R_{rs}^{-1}(687) - R_{rs}^{-1}(672)] \times [R(\lambda_4) - R(832)]$ and measured Chla when λ_4 is moved in the 600–900-nm range; (b) optimal correlation between $[R_{rs}^{-1}(687) - R_{rs}^{-1}(672)] \times [R^{-1}(600) - R^{-1}(832)]$ and measured Chla.

Figure 8 shows the turbidity results of the two-band model (T2) in SJNU and VDR. Figure 8a shows the correlation coefficient matrix between $[R_{rs}(\lambda_8)/R_{rs}(\lambda_9)]$ and measured turbidity. We obtained a relatively strong correlation only in the narrow area indicated by the area labeled “B” in the figure. Figure 8b shows the optimal correlation ($R^2 = 0.72$, RMSE = 257 NTU) between $[R_{rs}(821)/R_{rs}(763)]$ and

measured turbidity. SJNU data (10 NTU or less) do not appear to be detected in this model. Figure 8c,d shows RMSE variations between $[R_{rs}(\lambda_1)/R_{rs}(763)]$ or $[R_{rs}(821)/R_{rs}(\lambda_9)]$ and measured turbidity when λ_1 or λ_2 is in the 400–900-nm range. We obtained a low RMSE value in combination with 763 nm between 740 nm and 820 nm (RMSE = 400 NTU or less). In contrast, the band with low RMSE in combination with 821 nm is between 740 nm and 770 nm (RMSE = 400 NTU or less).

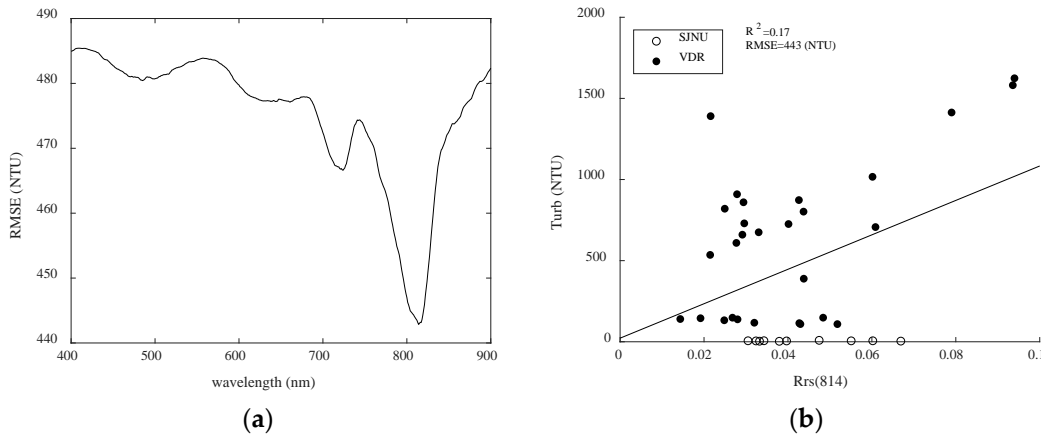


Figure 7. Turbidity results of the one-band model (T1) in SJNU and VDR. (a) Root mean square error variation between $R_{rs}^{-1}(\lambda_5)$ and measured turbidity when λ_5 is in the 400–900-nm range; (b) optimal correlation between $R_{rs}(814)$ and measured turbidity (Turb).

Figure 9 shows the turbidity results of the three-band model (T3) in SJNU and VDR. Figure 9a shows the RMSE variation between $R_{rs}(\lambda_8) - [R_{rs}(770) + R_{rs}(840)]/2$ and measured turbidity when λ_8 is in the 400–900-nm range. We obtained a relatively low RMSE (RMSE = 400 NTU or less) by tuning λ_8 between 780 nm and 840 nm. Figure 9b shows the RMSE variation between $R_{rs}(810) - [R_{rs}^{-1}(\lambda_9) + R_{rs}(840)]/2$ and measured turbidity when λ_9 is the 400–900-nm range and $R_{rs}(810) - [R_{rs}(770) + R_{rs}(\lambda_{10})]/2$ and measured turbidity when λ_{10} is in the 400–900-nm range. For λ_9 , we obtained a band with relatively low RMSE (RMSE = 300 NTU or less) between about 730 nm and 770 nm. In contrast, the relatively low RMSE (RMSE = 300 NTU or less) band for λ_{10} is between about 720 and 740 nm. Figure 9c shows the optimal correlation ($R^2 = 0.58$, RMSE = 316 NTU) between $R_{rs}(830) - [R_{rs}(770) + R_{rs}(840)]/2$ and measured turbidity. Figure 9d shows the optimal correlation ($R^2 = 0.70$, RMSE = 267 NTU) between $R_{rs}(810) - [R_{rs}(730) + R_{rs}(770)]$ and measured turbidity. Figure 9d seems to be more aggregated data of SJNU compared to Figure 9c.

Table 6 shows the optimal turbidity model using the T1, T2 and T3 models summarized above. Comparing RMSE values shows that the turbidity estimation error is small in the order of T2, T3 and T1.

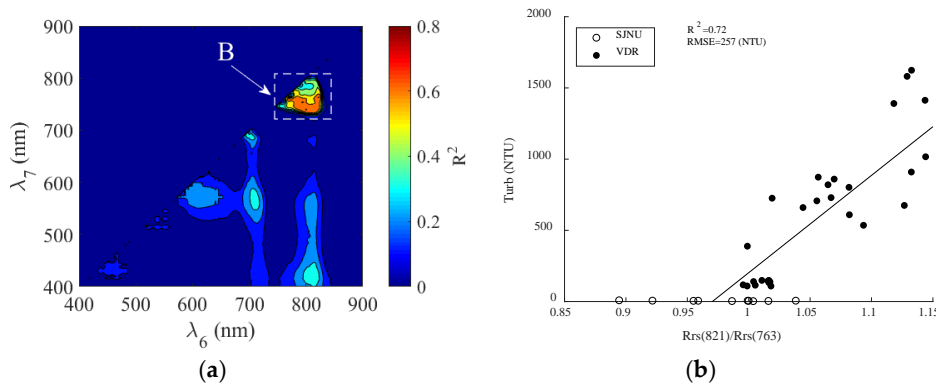


Figure 8. Cont.

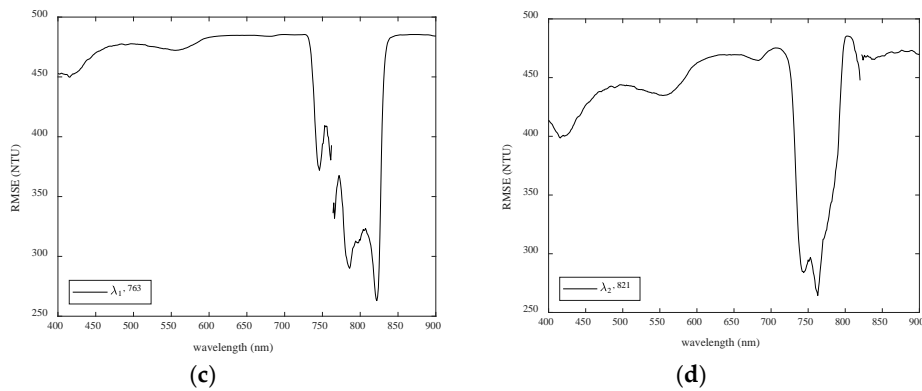


Figure 8. Turbidity results of the two-band model (T2) in SJNU and VDR. (a) Correlation coefficient matrix between $[R_{rs}(\lambda_8)/R_{rs}(\lambda_9)]$ and measured turbidity; (b) optimal correlation between $[R_{rs}(821)/R_{rs}(763)]$ and measured turbidity; (c) root mean square (RMSE) variation between $[R_{rs}(\lambda_1)/R_{rs}(763)]$ and measured turbidity when λ_1 is in the 400–900-nm range; (d) RMSE variation between $[R_{rs}(821)/R_{rs}(\lambda_9)]$ and measured turbidity when λ_2 is in the 400–900-nm range.

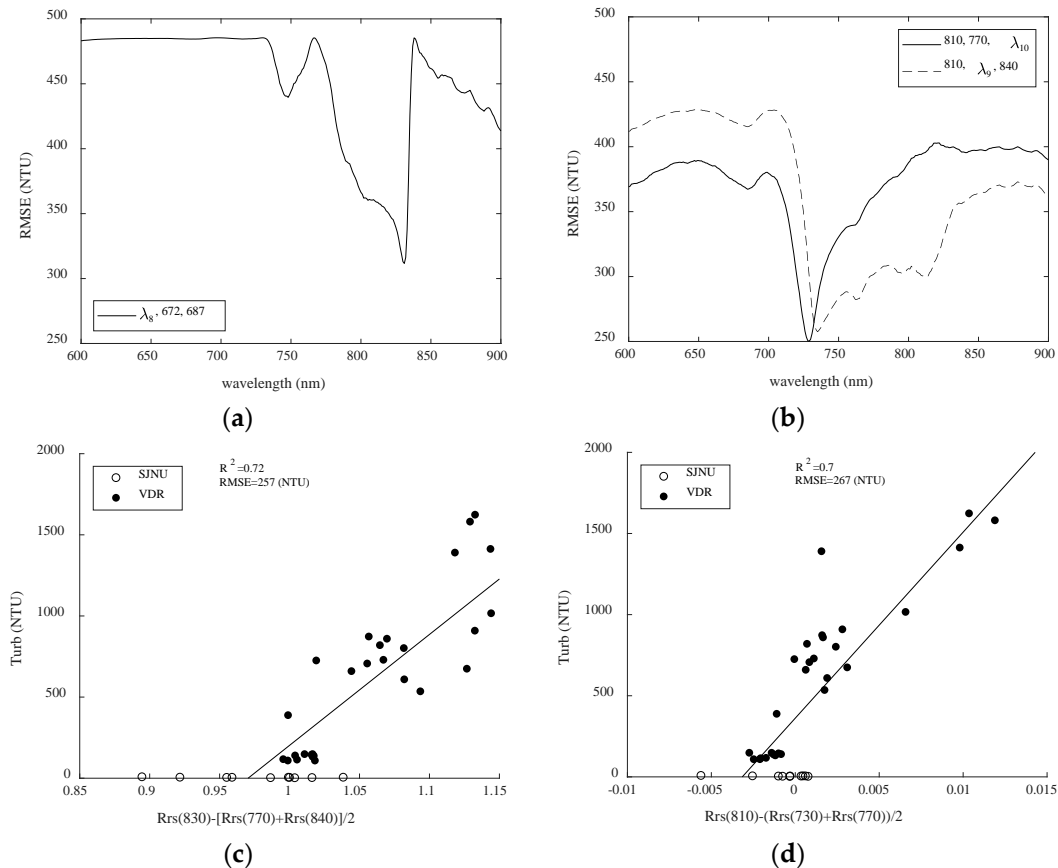


Figure 9. Turbidity results of the three-band model (T3) in SJNU and VDR. (a) Root mean square error (RMSE) variation between $R_{rs}(\lambda_8) - [R_{rs}(770) + R_{rs}(840)]/2$ and measured turbidity when λ_8 is in the 400–900-nm range; (b) RMSE variation between $R_{rs}(810) - [R_{rs}^{-1}(\lambda_9) + R_{rs}(840)]/2$ and measured turbidity when λ_9 is in the 400–900-nm range and $R_{rs}(810) - [R_{rs}(770) + R_{rs}(\lambda_{10})]/2$ and measured turbidity when λ_{10} is in the 400–900-nm range; (c) optimal correlation between $R_{rs}(830) - [R_{rs}(770) + R_{rs}^{-1}(840)]$ and measured turbidity; (d) optimal correlation between $R_{rs}(810) - [R_{rs}(730) + R_{rs}^{-1}(770)]$ and measured turbidity.

3.3. Algorithm Evaluation Using Simulated Sentinel-2 Data

We evaluated the Chla and turbidity algorithms for satellite observation bands (bands close to the tuned wavelength) using C1, C2, T2 and T3. Figure 10 shows Chla and turbidity results for the 2-BM and 3-BM using the Sentinel-2 MSI band only. Figure 10a shows the correlation between $R_{rs}(705)/R_{rs}(665)$ and measured Chla, and Figure 10b shows the correlation between $R_{rs}(775)/R_{rs}(740)$ and measured turbidity. Total R^2 was low at 0.25 and 0.49 for Chla and turbidity, respectively (RMSE: 3.1 mg m^{-3} and 347 NTU, respectively); however, R^2 slightly improved to 0.51 and 0.77 for Chla and turbidity, respectively (RMSE: 1.5 mg m^{-3} and 223 NTU, respectively) for the VDR. Figure 10c shows the correlation between $[R_{rs}^{-1}(705) - R_{rs}^{-1}(665)] \times R(842)$ and measured Chla, and Figure 10d shows the correlation between $R(810) - [R_{rs}(730) + R(770)]/2$ and measured turbidity. R^2 was not so high at 0.25 and 0.49 for Chla and turbidity, respectively (RMSE = 3.3 mg m^{-3} and 348 NTU, respectively). However, the correlation improved for the case of VDR data only.

Table 6. Optimal turbidity algorithm using the T1, T2 and T3 models.

Model		RMSE		
name	Algorithm	R^2	(NTU)	n
T1	$\text{Turb} = 10,613 \times R_{rs}(814) + 22.281$	0.17	443	38
T2	$\text{Turb} = 6834.7 \times R_{rs}(821)/R_{rs}(763) - 6632.2$	0.72	257	38
T3	$\text{Turb} = 114,642 \times (R_{rs}(810) - [R_{rs}(730) + R_{rs}(770)]/2) + 361.95$	0.70	267	38

Strong correlations cannot be obtained for all data, as shown in Figure 10a,b; however, the correlation becomes remarkably high only when data are confined to VDR. In such a case, VDR’s spectral reflectance characteristics can be determined mechanically and used as an algorithm with more versatility. We then examined spectral characteristics by separating data from SJNU and VDR. Figure 11a shows the average spectral reflectance characteristics (MSI band only) of all R_{rs} data in SJNU and VDR. Here, based on the shape of Slope 1 (the slope of R_{rs} at 705 nm and 740 nm), Slope 2 (the slope of R_{rs} at 775 nm and 865 nm) and Slope 3 (the slope of R_{rs} at 775 nm and 865 nm), we focused on the slope of R_{rs} between the bands. Figure 11b–d shows scatterplots for Slope 1 and Slope 2, Slope 1 and Slope 3 and Slope 2 and Slope 3, respectively. These figures make it clear that data from SJNU and VDR are clearly separated by slope combinations. In particular, in the Slope 1 and Slope 3 scatterplots shown in Figure 11b, SJNU and VDR data were clearly divided between the 1:1 line.

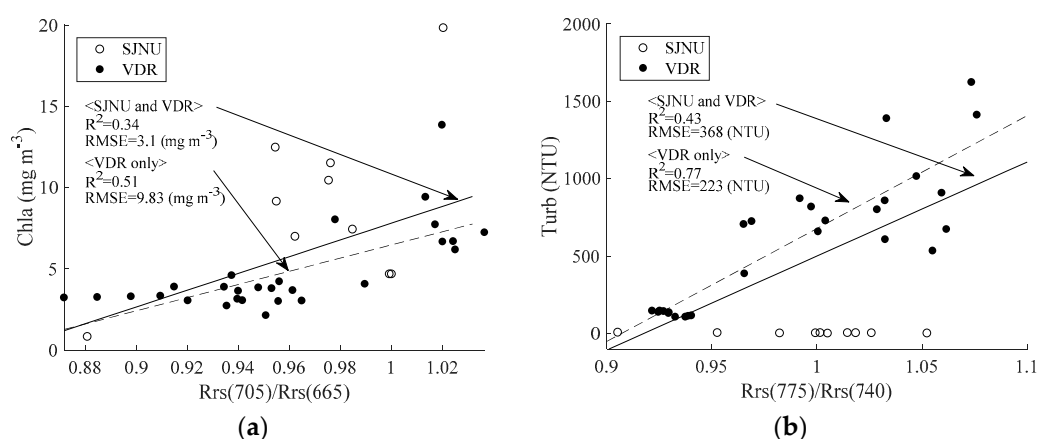


Figure 10. Cont.

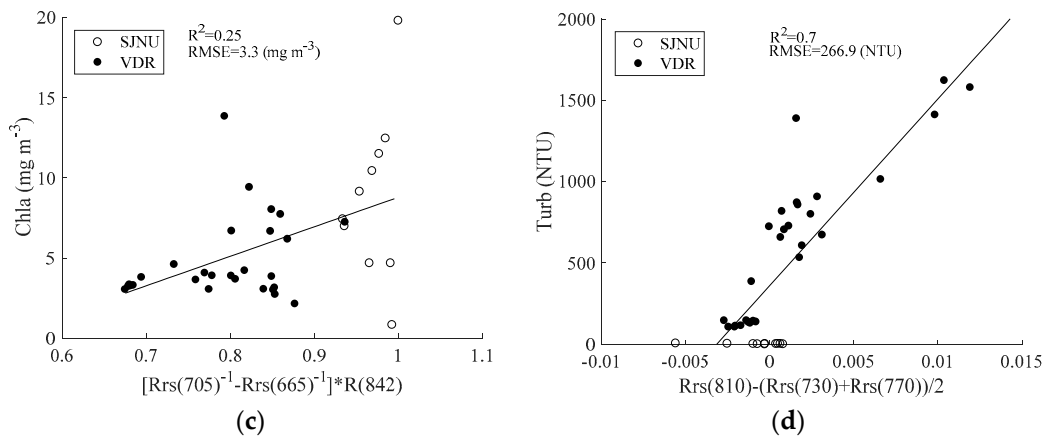


Figure 10. Chlorophyll a (Chla) and turbidity results for the two-band model and three-band model using the Sentinel-2 MSI band only. (a) Correlation between $R_{rs}(705)/R_{rs}(665)$ and measured Chla; (b) correlation between $R_{rs}(775)/R_{rs}(740)$ and measured turbidity; (c) correlation between $[R_{rs}^{-1}(705) - R_{rs}^{-1}(665)] \times R(842)$ and measured Chla; (d) correlation between $R(810) - [R_{rs}(730) + R(770)]/2$ and measured turbidity.

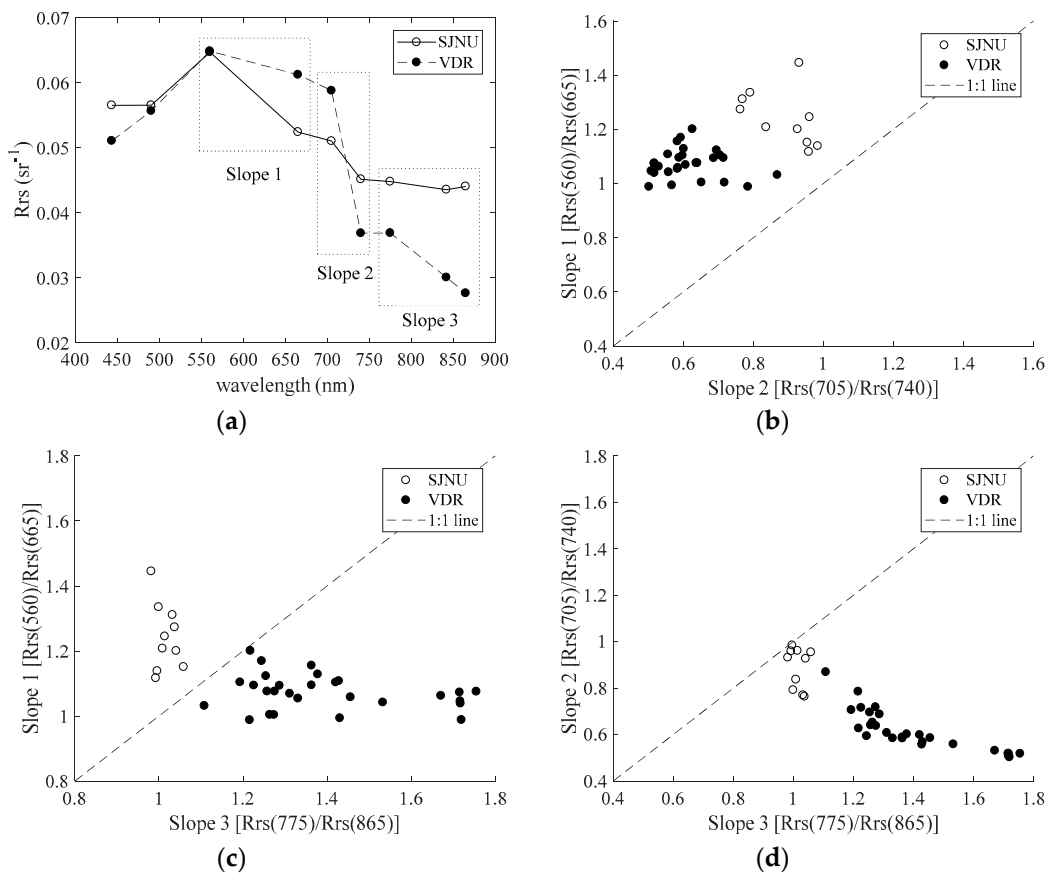


Figure 11. Separation method of the Lake Shinji and Lake Nakaumi (SJNU) and Vaal Dam Reservoir (VDR) types. (a) Average spectral reflectance (R_{rs}) characteristics (Multispectral Imager band only) of all R_{rs} data in SJNU and VDR; (b) relationship between Slope 1 ($R_{rs}(560)/R_{rs}(665)$) and Slope 2 ($R_{rs}(705)/R_{rs}(740)$); (c) relationship between Slope 1 ($R_{rs}(560)/R_{rs}(665)$) and Slope 3 ($R_{rs}(775)/R_{rs}(865)$); (d) relationship between Slope 2 ($R_{rs}(705)/R_{rs}(740)$) and Slope 3 ($R_{rs}(775)/R_{rs}(865)$).

4. Discussion

4.1. Evaluation of Chla Algorithm

As summarized in Table 5, we found the C1 and C2 models to be effective in estimating Chla at the two sites (R^2 is about 0.7, RMSE is about 2.0 mg m^{-3}). The four-band model, which is more suitable for detritus-rich water conditions, was found to not be significant under this study's conditions. We selected 672 nm and 687 nm as the optimal bands for the C1 model, adding 832 nm to these wavelengths for the C2 model. The wavelengths used in the C1 model for water on land were λ_1 (650–680 nm; red) and λ_2 (650–720 nm; near infra-red) for a Chla range of about $0\text{--}100 \text{ mg m}^{-3}$ [37–40]. Similarly, for the C2 model, λ_1 was 660–670 nm; λ_2 was 700–730 nm; and λ_3 was 740–760 nm [20,39,40]. The RMSE obtained in these past studies was about $8\text{--}10 \text{ mg m}^{-3}$ for a Chla range of $0\text{--}100 \text{ mg m}^{-3}$. The Chla range in our study was about one-fifth of those, so it is very harmonious that RMSE was around 2 mg m^{-3} . However, as seen in Figure 4, the wavelength range that can estimate Chla with such RMSE in an algorithm that can be used for both SJNU and VDR is very narrow (about $672 \pm 1 \text{ nm}$ and $687 \pm 1 \text{ nm}$).

4.2. Evaluation of Turbidity Algorithm

The T2 and T3 models were effective ($R^2 = 0.7$, RMSE = 260 NTU), as summarized in Table 6. Furthermore, we selected 821 nm and 763 nm as the optimal bands for T2 and 730 nm, 810 nm and 770 nm as the optimal bands for T3. In previous research, many models used a single band in the red to near-infrared as typified by Chen et al. [24], but when turbidity is extremely high and eutrophic, such as in a watershed, 2-BMs are often used. For example, the combination of 550 nm and 850 nm in France's Gironde Estuary (TSS: $13\text{--}985 \text{ g m}^{-3}$) by Doxaran et al. [27], that of 551 nm and 678 nm (MODIS Bands 12 and 14) in China's Yellow River (TSS: $2\text{--}1897 \text{ mg L}^{-1}$) by Qiu [41] and that of 555 nm and 645 nm in China's Yangtze River (TSS: $1\text{--}300 \text{ mg L}^{-1}$) by Hou et al. [42] were used for 2-BMs. These studies obtained very high correlations with R^2 values of 0.8 or more. Because our research sites also have extremely high turbidity and eutrophic water areas, the 2-BM seemed more suitable than a single-band model. Additionally, estimating only turbidity by using a near-infrared wavelength of about 740 nm or more, which is hardly affected by Chla absorption, can be considered appropriate as seen in Figure 1. In contrast, Kutser et al. [29] used bands of 770 nm, 810 nm and 840 nm (T3 model of this study), proposing a new 3-BM targeting the peak near 810 nm in CDOM-rich water areas. This method originally estimates the 810-nm height using the average height of 770 nm and 840 nm as a baseline. The result this time took the average value at 730 nm and 770 nm as the baseline; however, as this idea has just recently been announced, further discussion about which position to use as a baseline will be needed.

4.3. Feasibilities of Chla and Turbidity Estimation Using the Sentinel-2 MSI Band

In this study, we investigated whether Chla and turbidity can be estimated by MSI's band, assuming the recently-launched Sentinel-2 MSI, which has high spectral and spatial resolution. As shown in Figure 10, we found no correlation when using all data where both water zones were mixed such that R^2 was greater than 0.5 for both Chla and turbidity. However, when only the VDR data were used, we observed a significant correlation ($R^2 = 0.51$, RMSE = 9.8 mg m^{-3} , $N = 38$) in the 2-BM using 705 nm and 665 nm (MSI Bands 4 and 5). The 2-BM using 775 nm and 740 nm to measure turbidity found a significant correlation ($R^2 = 0.77$, RMSE = 223 NTU, $N = 38$). SJNU had much lower turbidity measurements than VDR; thus, we found it extremely difficult to find a unified algorithm. Recently, Chen et al. [43] conducted a Chla estimation study targeting MSI bands by measuring the spectral reflectance of Lake Huron (Chla range of $2\text{--}52 \text{ mg m}^{-3}$) obtaining 705 nm and 665 nm. In the 2-BM we used, we obtained a correlation of $R^2 = 0.49$ and RMSE = 9.97 mg m^{-3} . In addition, Ha et al. [44] obtained 2-BM R^2 values of 0.68 using 560 nm and 665 nm and $R^2 = 0.29$ using 705 nm

and 665 nm for Vietnam's Lake Ba Be (Chla range of 1–6 mg m⁻³). This difference indicates the 705-nm and 665-nm frequencies in the 2-BM as more effective in water areas with advanced eutrophication.

As described above, when the Chla and turbidity algorithms are only effective with VDR data, being able to limit the algorithms that can be used based on spectral characteristics beforehand is convenient. In this case, as shown in Figure 11, it is relatively easy to separate data using the spectral reflectance slope of the 2-BM (specifically the slope of MSI Bands 3 and 4 [$R_{rs}(560)$ and $R_{rs}(665)$] and the slope of MSI Bands 7 and 9 [$R_{rs}(775)$ and $R_{rs}(865)$]. Such spectroscopic separation is often used during remote sensing of red tide. For example, Takahashi et al. [45] proposed a method for separating red tide and non-red tide data by treating normalized water-leaving radiance spectral characteristics as almost equal to R_{rs} and using the slope of 443 nm and 490 nm and the slope of 490 nm and 555 nm, giving us a method to use. Although different from the subjects in this study, it can be said that the method for separating watershed properties using reflectance gradients can be used as a general and practical method in waters other than SJNU and VDR.

5. Conclusions

We acquired unified Chla and turbidity remote sensing algorithms based on recent Chla and turbidity algorithms using spectral reflectance data acquired by field surveys of SJNU and VDR and evaluating significantly different spectral characteristics. In addition, we also considered Chla and turbidity estimation using Sentinel-2 MSI frequency bands. As a result, we clarified the following items.

1. As a unified Chla model in SJNU and VDR, we obtained strong correlation ($R^2 =$ about 0.7, RMSE = 2 mg m⁻³, N = 38) between $R_{rs}(687)/R_{rs}(672)$ (2-BM) or $[R_{rs}^{-1}(687) - R_{rs}^{-1}(672)] \times R_{rs}(832)$ (3-BM) and estimated Chla.
2. As a unified turbidity model in SJNU and VDR, we obtained strong correlation ($R^2 =$ about 0.7, RMSE = about 260 NTU, N = 38) between $R_{rs}(763)/R_{rs}(821)$ (2-BM) or $R_{rs}(810) - [R_{rs}(730) + R_{rs}(770)]/2$ (3-BM) and estimated turbidity.
3. As a Chla model confined to the MSI frequency band, we obtained strong correlation ($R^2 =$ 0.51, RMSE = 9.8 mg m⁻³, N = 28) between 2-BM using MSI Bands 4 and 5 ($R_{rs}(740)$ and $R_{rs}(775)$) and estimated turbidity.
4. As a turbidity model confined to the MSI frequency band, we obtained strong correlation ($R^2 =$ 0.77, RMSE = 0.77, 223 NTU, N = 28) between 2-BM using MSI Bands 6 and 7 ($R_{rs}(740)$ and $R_{rs}(775)$) and estimated turbidity.
5. The method using the slopes of $R_{rs}(560)$ and $R_{rs}(665)$ and the slopes of $R_{rs}(775)$ and $R_{rs}(865)$ (that is, judgment above and below the 1:1 line) was effective at spectrally separating SJNU data and VDR data.

Validation of these models by applying them to actual MSI data is a crucial step in assessing model viability and accuracy using space-borne satellite images. Additionally, continuous monitoring of water quality changes in the VDR and SJNU through mapping will help dam water management.

Author Contributions: Y.S. was the director of the field survey and this paper. H.Y. and M.A.M.A.E. were the project leaders in the planning and implementation of field campaigns for this research project. Y.Y., S.S., E.A. and J.G.C. performed the field survey execution and analysis, respectively.

Acknowledgments: This study was supported in part by JSPS/NRF (National Research Foundation) Bilateral Joint Research Project, "Future scenarios of Japan and South Africa surface water quality: Under changing climate and land-use" and by JSPS KAKENHI (16H05631 and 17H04625).

Conflicts of Interest: The authors declare no conflict of interest.

Appendix A

Table A1. The summary of dataset used in this study. The R_{rs} is shown for the Sentinel-2 MSI band only.

Date	Station	Chla (mg m ⁻³)	Turb (NTU)	R_{rs} (nm) × 10 ⁻⁵							
				443	490	560	705	740	775	842	865
15 July 2016	SJNU										
	S-6	19.7	3	4093	3859	4199	3547	2969	2974	2977	2947
	S-3	6.0	3	6465	6248	6942	6212	5957	6044	6012	6086
	S-1	7.4	3	5669	5591	6660	5851	5759	5867	5685	5887
	N-6	9.1	2	5137	4866	5736	4400	4228	4225	4039	4165
	N-1	7.7	6	5446	5694	6948	5945	5675	5138	4814	4851
	Ohashi-Mid	6.8	3	4463	4553	5301	4249	3938	3752	3518	3602
12 September 2016	SJNU										
	S-6	12.2	2	4685	4801	5593	3999	3166	3249	3204	3250
	S-3	11.5	1	9472	9614	11,007	8440	6444	6331	6220	6100
	S-1	10.4	0	5526	5587	6516	4848	3731	3750	3641	3632
	Ohashi-Mid	0.8	1	5573	5731	5796	3533	3290	3463	3443	3526
28 October 2016	VDR										
	Stn3	3.2	386	7042	6959	7176	6163	4409	4258	3642	3472
	Stn4	2.9	704	7279	7918	9215	8773	5723	5525	4728	4370
	Stn5	2.5	857	3946	4050	4349	3746	2644	2730	2397	2287
	Stn6	3.7	870	5785	6143	6884	6067	3866	3836	3266	3007
	Stn7	3.1	657	4511	4551	4724	3936	2738	2740	2341	2183
	Stn8	4.0	817	4108	4240	4587	3799	2286	2280	1829	1654
	Stn9	2.9	727	4767	5123	5791	4811	2678	2689	2087	1883
	Stn13	7.2	1578	7689	8073	8725	8767	7619	8382	7908	7561
	Stn14	6.1	1621	7892	8496	9627	9990	7845	8422	7374	6924
	Stn15	6.7	1410	6723	7517	8744	8887	6383	6869	5860	5390
	Stn16	9.6	1014	6136	7255	9058	8475	4987	5224	4207	3831
	Stn17	2.9	799	6007	6338	6941	6077	3892	4004	3372	3183
	Stn18	3.9	672	3610	4169	5165	4710	2751	2921	2359	2194
	Stn19	4.4	533	2612	2892	3402	3043	1848	1950	1595	1487
	Stn20	13.7	1388	2627	2903	3569	3150	1839	1900	1508	1393
	Stn21	10.6	606	3836	4075	4603	3899	2443	2523	2172	2072
	Stn22	9.2	906	3753	4057	4659	3897	2313	2451	2083	1969
	Stn23	11.3	723	5314	5529	6154	5703	3920	3799	3133	2951
27 March 2017	VDR										
	Stn.21	4.5	106	6059	6986	8588	7727	4315	4046	2977	2639
	Stn.22	3.9	106	7063	7948	9715	8948	5083	4741	3709	3313
	Stn.16	3.7	114	4815	5263	6250	5553	3251	3057	2325	2099
	Stn.15	4.0	112	5980	6572	7966	7144	4276	4015	3100	2826
	New-1	3.8	130	3682	4145	5188	4654	2469	2295	1596	1373
	Stn.17	3.7	135	4078	4669	5940	5331	2761	2567	1736	1462
	Stn.8	3.3	146	4433	4931	6027	5241	2668	2468	1682	1437
	Stn.4	3.3	142	3201	3543	4265	3687	1909	1770	1213	1031
	Stn.3'	3.2	137	2854	2974	3382	2789	1444	1335	910	778
	New-2	3.2	146	7172	8525	10,916	9631	4840	4461	3044	2594

References

- Shiklomanov, I.A. *World Water Resources. A New Appraisal and Assessment for the 21st Century*; UNESCO: Paris, France, 1998.
- Simis, S.G.; Ruiz-Verdú, A.; Domínguez-Gómez, J.A.; Peña-Martínez, R.; Peters, S.W.; Gons, H.J. Influence of phytoplankton pigment composition on remote sensing of cyanobacterial biomass. *Remote Sens. Environ.* **2007**, *106*, 414–427. [[CrossRef](#)]
- Yamamoto, M.; Koike, I. Diel changes of nitrogen species in surface and overlying water of an estuarine lake in summer: Evidence for benthic-pelagic coupling. *Limnol. Oceanogr.* **1994**, *39*, 1726–1733. [[CrossRef](#)]
- Nakamura, Y.; Kerciku, F. Effects of filter-feeding bivalves on the distribution of water quality and nutrient cycling in a eutrophic coastal lagoon. *J. Mar. Syst.* **2000**, *26*, 209–221. [[CrossRef](#)]
- Uye, S.; Shimazu, T.; Yamamoto, M.; Ishitobi, Y.; Kamiya, H. Geographical and seasonal variations in mesozooplankton abundance and biomass in relation to environmental parameters in Lake Shinji–Ohashi River–Lake Nakaumi brackish-water system, Japan. *J. Mar. Syst.* **2000**, *26*, 193–207. [[CrossRef](#)]
- Kunii, H.; Minamoto, K. Temporal and spatial variation in the macrophyte distribution in coastal lagoon Lake Nakaumi and its neighboring waters. *J. Mar. Syst.* **2000**, *26*, 223–231. [[CrossRef](#)]

7. Senga, Y.; Seike, Y.; Mochida, K.; Fujinaga, K.; Okumura, M. Nitrous oxide in brackish lakes Shinji and Nakaumi, Japan. *Limnology* **2001**, *2*, 129–136. [[CrossRef](#)]
8. Yamamuro, M.; Hiratsuka, J.I.; Ishitobi, Y.; Hosokawa, S.; Nakamura, Y. Ecosystem shift resulting from loss of eelgrass and other submerged aquatic vegetation in two estuarine lagoons, Lake Nakaumi and Lake Shinji, Japan. *J. Oceanogr.* **2006**, *62*, 551–558. [[CrossRef](#)]
9. Sugahara, S.; Kamiya, H.; Suyama, Y.; Senga, Y.; Ayukawa, K.; Okumura, M.; Seike, Y. Influence of hypersaturated dissolved oxygenated water on the elution of hydrogen sulfide and methane from sediment in the dredged area in polyhaline Lake Nakaumi. *Landsc. Ecol. Eng.* **2015**, *11*, 269–282. [[CrossRef](#)]
10. Taylor, J.C.; van Vuuren, M.J.; Pieterse, A.J.H.; Kriel, J.P. The role of tile Hendrik Verwoerd Dam in the Orange River Project. *Civ. Eng. = Siviele Ingenieurswese* **1972**, *14*, 51–61.
11. Braune, E.; Rogers, K.H. *Vaal River Catchment: Problems and Research Needs*; National Scientific Programmes Unit; CSIR: Pretoria, South Africa, 1987.
12. Grobler, D.C.; Toerien, D.F.; Rossouw, J.N. A review of sediment/water quality interaction with particular reference to the Vaal River system. *Water S. Afr.* **1987**, *13*, 15–22.
13. Taylor, J.C.; van Vuuren, M.J.; Pieterse, A.J.H. The application and testing of diatom-based indices in the Vaal and Wilge Rivers, South Africa. *Water S. Afr.* **2007**, *33*, 51–59. [[CrossRef](#)]
14. Naicker, K.; Cukrowska, E.; McCarthy, T.S. Acid mine drainage arising from gold mining activity in Johannesburg, South Africa and environs. *Environ. Pollut.* **2003**, *122*, 29–40. [[CrossRef](#)]
15. McCarthy, T.S. The impact of acid mine drainage in South Africa. *S. Afr. J. Sci.* **2011**, *107*, 1–7. [[CrossRef](#)]
16. Jury, M.R. Economic impacts of climate variability in South Africa and development of resource prediction models. *J. Appl. Meteorol.* **2002**, *41*, 46–55. [[CrossRef](#)]
17. Matthews, M.W. A current review of empirical procedures of remote sensing in inland and near-coastal transitional waters. *Int. J. Remote Sens.* **2011**, *32*, 6855–6899. [[CrossRef](#)]
18. Mittenzwey, K.H.; Ullrich, S.; Gitelson, A.A.; Kondratiev, K.Y. Determination of chlorophyll a of inland waters on the basis of spectral reflectance. *Limnol. Oceanogr.* **1992**, *37*, 147–149. [[CrossRef](#)]
19. Gitelson, A.A. The peak near 700 nm on radiance spectra of algae and water: Relationships of its magnitude and position with chlorophyll concentration. *Int. J. Remote Sens.* **1992**, *13*, 3367–3373. [[CrossRef](#)]
20. Dall’Olmo, G.; Gitelson, A.A. Effect of bio-optical parameter variability on the remote estimation of chlorophyll-a concentration in turbid productive waters: Experimental results. *Appl. Opt.* **2005**, *44*, 412–422. [[CrossRef](#)] [[PubMed](#)]
21. Yang, W.; Matsushita, B.; Chen, J.; Fukushima, T. Estimating constituent concentrations in case II waters from MERIS satellite data by semi-analytical model optimizing and look-up tables. *Remote Sens. Environ.* **2011**, *115*, 1247–1259. [[CrossRef](#)]
22. Le, C.; Li, Y.; Zha, Y.; Sun, D.; Huang, C.; Lu, H. A four-band semi-analytical model for estimating chlorophyll a in highly turbid lakes: The case of Taihu Lake, China. *Remote Sens. Environ.* **2009**, *113*, 1175–1182. [[CrossRef](#)]
23. Le, C.; Hu, C.; Cannizzaro, J.; English, D.; Muller-Karger, F.; Lee, Z. Evaluation of chlorophyll-a remote sensing algorithms for an optically complex estuary. *Remote Sens. Environ.* **2013**, *129*, 75–89. [[CrossRef](#)]
24. Chen, Z.; Hu, C.; Muller-Karger, F. Monitoring turbidity in Tampa Bay using MODIS/Aqua 250-m imagery. *Remote Sens. Environ.* **2007**, *109*, 207–220. [[CrossRef](#)]
25. Nechad, B.; Ruddick, K.G.; Park, Y. Calibration and validation of a generic multisensor algorithm for mapping of total suspended matter in turbid waters. *Remote Sens. Environ.* **2010**, *114*, 854–866. [[CrossRef](#)]
26. Kallio, K.; Kutser, T.; Hannonen, T.; Koponen, S.; Pulliainen, J.; Vepsäläinen, J.; Pyhälähti, T. Retrieval of water quality from airborne imaging spectrometry of various lake types in different seasons. *Sci. Total Environ.* **2001**, *268*, 59–77. [[CrossRef](#)]
27. Doxaran, D.; Froidefond, J.M.; Castaing, P.; Babin, M. Dynamics of the turbidity maximum zone in a macrotidal estuary (the Gironde, France): Observations from field and MODIS satellite data. *Estuar. Coast. Shelf Sci.* **2009**, *81*, 321–332. [[CrossRef](#)]
28. Letelier, R.M.; Abbott, M.R. An analysis of chlorophyll fluorescence algorithms for the Moderate Resolution Imaging Spectrometer (MODIS). *Remote Sens. Environ.* **1996**, *58*, 215–223. [[CrossRef](#)]
29. Kutser, T.; Paavel, B.; Verpoorter, C.; Ligi, M.; Soomets, T.; Toming, K.; Casal, G. Remote sensing of black lakes and using 810 nm reflectance peak for retrieving water quality parameters of optically complex waters. *Remote Sens.* **2016**, *8*, 497. [[CrossRef](#)]

30. Shen, F.; Zhou, Y.X.; Li, D.J.; Zhu, W.J.; Suhyb Salama, M. Medium resolution imaging spectrometer (MERIS) estimation of chlorophyll-a concentration in the turbid sediment-laden waters of the Changjiang (Yangtze) Estuary. *Int. J. Remote Sens.* **2010**, *31*, 4635–4650. [[CrossRef](#)]
31. Hu, C.; Chen, Z.; Clayton, T.D.; Swarzenski, P.; Brock, J.C.; Muller-Karger, F.E. Assessment of estuarine water-quality indicators using MODIS medium-resolution bands: Initial results from Tampa Bay, FL. *Remote Sens. Environ.* **2004**, *93*, 423–441. [[CrossRef](#)]
32. Matthews, M.W.; Bernard, S.; Winter, K. Remote sensing of cyanobacteria-dominant algal blooms and water quality parameters in Zeekoevlei, a small hypertrophic lake, using MERIS. *Remote Sens. Environ.* **2010**, *114*, 2070–2087. [[CrossRef](#)]
33. Olmanson, L.G.; Brezonik, P.L.; Bauer, M.E. Airborne hyperspectral remote sensing to assess spatial distribution of water quality characteristics in large rivers: The Mississippi River and its tributaries in Minnesota. *Remote Sens. Environ.* **2013**, *130*, 254–265. [[CrossRef](#)]
34. Oyama, Y.; Matsushita, B.; Fukushima, T.; Matsushige, K.; Imai, A. Application of spectral decomposition algorithm for mapping water quality in a turbid lake (Lake Kasumigaura, Japan) from Landsat TM data. *ISPRS J. Photogramm. Remote Sens.* **2009**, *64*, 73–85. [[CrossRef](#)]
35. Mobley, C.D. Estimation of the remote-sensing reflectance from above-surface measurements. *Appl. Opt.* **1999**, *38*, 7442–7455. [[CrossRef](#)] [[PubMed](#)]
36. Tan, J.; Cherkauer, K.A.; Chaubey, I. Using hyperspectral data to quantify water-quality parameters in the Wabash River and its tributaries, Indiana. *Int. J. Remote Sens.* **2015**, *36*, 5466–5484. [[CrossRef](#)]
37. Oki, K.; Yasuoka, Y.; Tamura, Y. Estimation of chlorophyll-a and suspended solids concentration in rich concentration water area with remote sensing technique. *J. Remote Sens. Soc. Jpn.* **2001**, *21*, 449–457.
38. Thiemann, S.; Kaufmann, H. Lake water quality monitoring using hyperspectral airborne data—A semiempirical multisensor and multitemporal approach for the Mecklenburg Lake District, Germany. *Remote Sens. Environ.* **2002**, *81*, 228–237. [[CrossRef](#)]
39. Gitelson, A.A.; Schalles, J.F.; Hladik, C.M. Remote chlorophyll-a retrieval in turbid, productive estuaries: Chesapeake Bay case study. *Remote Sens. Environ.* **2007**, *109*, 464–472. [[CrossRef](#)]
40. Zimba, P.V.; Gitelson, A. Remote estimation of chlorophyll concentration in hyper-eutrophic aquatic systems: Model tuning and accuracy optimization. *Aquaculture* **2006**, *256*, 272–286. [[CrossRef](#)]
41. Qiu, Z. A simple optical model to estimate suspended particulate matter in Yellow River Estuary. *Opt. Express* **2013**, *21*, 27891–27904. [[CrossRef](#)] [[PubMed](#)]
42. Hou, X.; Feng, L.; Duan, H.; Chen, X.; Sun, D.; Shi, K. Fifteen-year monitoring of the turbidity dynamics in large lakes and reservoirs in the middle and lower basin of the Yangtze River, China. *Remote Sens. Environ.* **2017**, *190*, 107–121. [[CrossRef](#)]
43. Chen, J.; Zhu, W.; Tian, Y.Q.; Yu, Q.; Zheng, Y.; Huang, L. Remote estimation of colored dissolved organic matter and chlorophyll-a in Lake Huron using Sentinel-2 measurements. *J. Appl. Remote Sens.* **2017**, *11*, 036007. [[CrossRef](#)]
44. Ha, N.T.T.; Thao, N.T.P.; Koike, K.; Nhuan, M.T. Selecting the Best Band Ratio to Estimate Chlorophyll-a Concentration in a Tropical Freshwater Lake Using Sentinel 2A Images from a Case Study of Lake Ba Be (Northern Vietnam). *ISPRS Int. J. Geo-Inf.* **2017**, *6*, 290. [[CrossRef](#)]
45. Takahashi, W.; Kawamura, H.; Omura, T.; Furuya, K. Detecting red tides in the eastern Seto inland sea with satellite ocean color imagery. *J. Oceanogr.* **2009**, *65*, 647–656. [[CrossRef](#)]

